PHYSICS

The spin Hall effect of Bi-Sb alloys driven by thermally excited Dirac-like electrons

Zhendong Chi[1,2], Yong-Chang Lau[1,2,3]*, Xiandong Xu[2], Tadakatsu Ohkubo[2], Kazuhiro Hono[2], Masamitsu Hayashi[1,2]*

We have studied the charge to spin conversion in $Bi_{1-x}Sb_x$/CoFeB heterostructures. The spin Hall conductivity (SHC) of the sputter-deposited heterostructures exhibits a high plateau at Bi-rich compositions, corresponding to the topological insulator phase, followed by a decrease of SHC for Sb-richer alloys, in agreement with the calculated intrinsic spin Hall effect of $Bi_{1-x}Sb_x$. The SHC increases with increasing $Bi_{1-x}Sb_x$ thickness before it saturates, indicating that it is the bulk of the alloy that predominantly contributes to the generation of spin current; the topological surface states, if present, play little role. Unexpectedly, the SHC is found to increase with increasing temperature, following the trend of carrier density. These results suggest that the large SHC at room temperature, with a spin Hall efficiency exceeding 1 and an extremely large spin current mobility, is due to increased number of thermally excited Dirac-like electrons in the *L* valley of the narrow gap $Bi_{1-x}Sb_x$ alloy.

INTRODUCTION

Generation of spin current or flow of spin angular momentum lies at the heart of modern spintronics. The power consumption of a spintronic device is directly related to its efficiency for converting a charge current that dissipates energy to a dissipative spin-polarized current or a dissipationless spin current (*1*, *2*). A conventional means for creating a flow of spin angular momentum is by passing a charge current across a ferromagnetic metal (FM) that converts to a spin-polarized current. The efficacy of this process is proportional to the spin polarization of the FM. More recently, generation of spin current from a charge current passed along a nonmagnetic metal (NM) (*3*–*5*) or interface of materials with strong spin-orbit coupling (*6*–*8*) has emerged as an attractive alternative. In particular, the discovery (*9*) of the giant spin Hall effect (SHE) in 5*d* transition heavy metals (HMs) has triggered substantial effort in exploiting the spin current to electrically control magnetization of ferromagnets placed nearby. In HM/FM bilayer systems, the magnetization of the FM layer can absorb the orthogonal component of the nonequilibrium spin density originating from the SHE, giving rise to current-induced spin-orbit torque (SOT) at the HM/FM interface (*10*–*12*). The SOT in these bilayers enabled current-induced magnetization switching (*9*, *13*), current-driven motion of chiral domain walls and skyrmions (*14*–*16*), and magnetoresistance (MR) effect that depends on the SHE, often referred to as the spin Hall MR (*17*, *18*). The figure of merit of the charge to spin conversion in SHE is known as the damping-like spin Hall efficiency ξ_{DL} that includes nonideal spin transmission across the interface (*19*, *20*). Using ξ_{DL}, the spin current j_s generated from a charge current j_c passed to an NM layer and entering the FM layer can be expressed as $j_s = \xi_{DL}(\hbar/2e)j_c$, where $\hbar$ is the reduced Planck constant and e is the electrical charge. As ξ_{DL} may depend on the longitudinal conductivity σ_{xx} of the NM layer, which varies with extrinsic factors such as impurity concentration and film texture, it is customary to use the spin Hall conductivity (SHC) σ_{SH}, defined through the relation $\sigma_{SH} = \xi_{DL} \cdot \sigma_{xx}$, to provide a measure of the anomalous transverse velocity the carriers obtain via the SHE (*5*).

Recent advances in the understanding of topological insulators (*21*) and Weyl semimetals (*22*) have attracted great interest in exploiting their unique electronic states for spintronic applications. Giant charge to spin conversion efficiencies were found in heterostructures that consist of a topological insulator and a ferromagnetic/ferrimagnetic layer (*23*–*32*). The large charge to spin conversion efficiency observed in these systems was attributed to the current-induced generation of spin density enabled by the spin momentum locked surface states of topological insulators. Ideally, the bulk of a topological insulator should be insulating. In practice, however, it remains as a great challenge to limit the current flow within the bulk of this material class. This is particularly the case for thin-film heterostructures in which imperfect crystal structures and interdiffusion with the adjacent layers may reduce or eliminate the bandgap of the bulk state. To take advantage of the topological surface states in generating spin accumulation, it has been considered detrimental to have current paths in the bulk. In terms of bulk conduction of carriers, the charge to spin conversion efficiency of Bi, a small gap semimetal with large spin-orbit coupling (*33*, *34*) and one of the most used elements in forming topological insulators, has been reported to be extremely small (*35*, *36*) compared to the 5*d* transition metals. Theoretically, Bi and Bi-Sb alloys have been predicted (*37*–*39*) to exhibit considerable SHC due to its unique electronic state.

Here, we show that the charge to spin conversion efficiency that originates from the bulk of $Bi_{1-x}Sb_x$ alloys is significantly larger than that of the 5*d* transition metals. The SHC of the alloy increases with increasing thickness before it saturates. This thickness dependence of the SHC, together with its facet independence, suggests that a significant amount of spin current is generated from the bulk of the alloy. We find little evidence of spin current generation from the topological surface states, if they were to exist in the sputtered films used here. The damping-like spin Hall efficiency exceeds 1 for the Bi-rich $Bi_{1-x}Sb_x$ alloy and decreases with increasing Sb concentration. The alloy composition dependence of the SHC indicates that the SHE of the alloy has considerable contribution from the so-called intrinsic SHE. Unexpectedly, we find that the SHC and the spin Hall efficiency increase with increasing measurement temperature. We find up to

[1]Department of Physics, The University of Tokyo, Bunkyo-ku, Tokyo 113-0033, Japan. [2]National Institute for Materials Science, Tsukuba, Ibaraki 305-0047, Japan. [3]Institute for Materials Research (IMR), Tohoku University, Sendai 980-8577, Japan.
*Corresponding author. Email: yongchang.lau@qspin.phys.s.u-tokyo.ac.jp (Y.-C.L.); hayashi@phys.s.u-tokyo.ac.jp (M.H.)

threefold (twofold) enhancement of σ_{SH} (ξ_{DL}) upon increasing the temperature from 10 to 300 K. Although thermal fluctuation is typically detrimental for many key parameters of spintronic devices, the SHC of the $Bi_{1-x}Sb_x$ alloy is enhanced at higher temperature due to the increased number of carriers at the valleys with large Berry curvature. Our results suggest that these carriers in $Bi_{1-x}Sb_x$ alloys, particularly in the Bi-rich compositions, have large spin current generation efficiency and equivalent spin current mobility.

RESULTS

Structural characterizations

Thin-film heterostructures with base structure of Sub./seed/[t_{Bi} Bi | t_{Sb} Sb]$_N$/t_{Bi} Bi/t_{CoFeB} CoFeB/2 MgO/1 Ta (thicknesses in nanometers) were grown by magnetron sputtering at ambient temperature on thermally oxidized Si substrates. N represents the number of repeats of the Bi | Sb bilayers. The thicknesses of the Bi (t_{Bi}) and Sb (t_{Sb}) layers in the repeated structure are set to meet the condition t_{Bi} + t_{Sb} ~ 0.7 nm. The nominal composition of CoFeB is Co:Fe:B = 20:60:20 atomic %. Unless noted otherwise, we use 0.5 nm Ta as the seed layer for Bi|Sb multilayers. The capping layer is always fixed to 2 MgO/1 Ta. We assume that the top 1-nm Ta layer is fully oxidized and does not contribute to the transport properties of the films.

θ – 2θ x-ray diffraction (XRD) spectra of representative films with t_{Bi} ~ t_{Sb} ~ 0.35 nm, N = 8, 16 are shown in Fig. 1A. The films are polycrystalline, and the peaks are indexed on the basis of the hexagonal representation of the rhombohedral $Bi_{1-x}Sb_x$ (space group $R\bar{3}m$; no. 166) that forms solid solution throughout the composition. Bragg diffraction peaks corresponding to (0003), (01$\bar{1}$2), and (10$\bar{1}$4) crystallographic directions are found. The peak intensities increase with increasing N, reflecting improved crystallinity of the film. Atomic force microscopy (AFM) image of the N = 8 film is shown in Fig. 1B. The root mean square roughness is of the order of 1 nm. Representative cross sectional high-angle annular dark-field scanning transmission electron microscopy (HAADF-STEM) images of the N = 16 film are shown in Fig. 1C. The lower-magnification STEM image at the top panel confirms that the Bi|Sb multilayer is granular and continuous. We find that the average grain size is ~35 nm. The 2-nm CoFeB and the subsequent capping layers are also continuous and follow the morphology of the multilayer. The bottom panel shows the high-resolution STEM image of the film. The lattice fringes clearly seen in the image reveals the good crystallinity of the Bi|Sb multilayer. A typical nanobeam diffraction pattern of the Bi|Sb multilayer is shown in the inset of Fig. 1C. The diffraction patterns suggest that the grains are consisted of $Bi_{1-x}Sb_x$ nanocrystallites with random orientations within the film plane. Although alternating Bi and Sb layers were sputtered to form Bi|Sb multilayers, energy-dispersive x-ray spectroscopy (EDS) mapping (see the Supplementary Materials) shows that the two elements intermix to form an alloy rather than a layer-by-layer superlattice.

Experimental setup

Because structural characterization show that the two elements intermix and form an alloy, we denote, hereafter, the Bi|Sb multilayers (i.e., [t_{Bi} Bi| t_{Sb} Sb]$_N$/t_{Bi} Bi) as t_{BiSb} $Bi_{1-x}Sb_x$ using the total thickness of the multilayer (t_{BiSb}) and the corresponding composition x defined by the relative thickness of the Bi and Sb layers, i.e., $x \equiv \frac{t_{Sb}}{t_{Bi}+t_{Sb}}$. To evaluate the SOT, we pattern Hall bar devices using optical lithography. The nominal channel width w and length L are set to 10 and 25 μm, respectively. Illustration of the Hall bar device and the coordinate system adapted in this work are schematically illustrated in the inset of Fig. 2A. The longitudinal resistance R_{xx} and the transverse resistance R_{xy} of the devices were obtained using direct current (DC) transport measurements. Linear fitting to the sheet conductance $L/(wR_{xx})$ versus the thickness of one of the layers is used to estimate the conductivity σ_X (X = BiSb, CoFeB, seed layer). The current distribution within the heterostructures is calculated using the thicknesses and conductivities of the conducting layers.

We use the harmonic Hall technique (*11*, *12*, *40*–*42*) to quantify the SOT of in-plane magnetized $Bi_{1-x}Sb_x$/CoFeB heterostructures. Upon application of an alternating current (AC) I_0 sin ωt with frequency ω/2π and amplitude I_0 along x, an external magnetic field H_{ext} is applied in the xy plane, while the in-phase first harmonic ($V_{1\omega}$) and the out-of-phase second harmonic ($V_{2\omega}$) Hall voltages along y are simultaneously measured. The Hall resistance is obtained by dividing the harmonic voltages with I_0, i.e., $R_{1\omega(2\omega)} \equiv V_{1\omega(2\omega)}/(I_0/\sqrt{2})$. $R_{1\omega}$ is dominated by the planar Hall and anomalous Hall resistances, whereas $R_{2\omega}$ contains contributions from the current-induced damping-like spin-orbit effective field (H_{DL}), the field-like spin-orbit effective field (H_{FL}), the Oersted field (H_{Oe}), and thermoelectric effects [anomalous Nernst effect (ANE) of CoFeB, the ordinary Nernst effect (ONE) of $Bi_{1-x}Sb_x$ (*43*), and the collective action of the spin Seebeck effect (SSE) in CoFeB followed by the inverse SHE (ISHE) in $Bi_{1-x}Sb_x$ (*41*)]. The magnetic field amplitude dependence of $R_{2\omega}$ allows one to differentiate

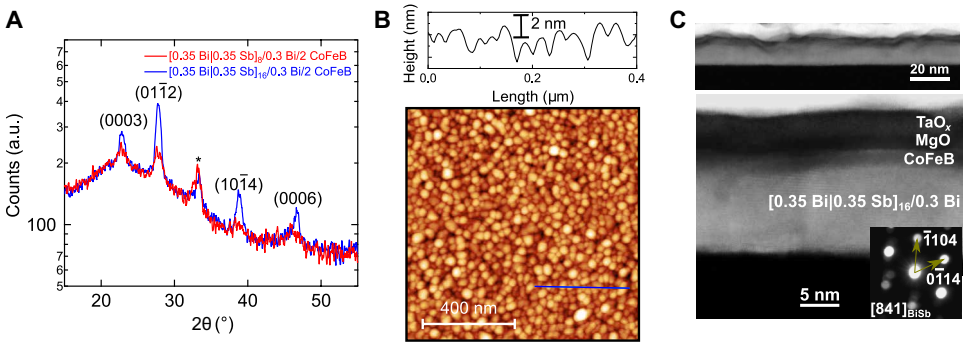

Fig. 1. Structural characterization of Bi|Sb multilayers. (**A**) X-ray diffraction (XRD) spectra of 0.5 Ta/[0.35 Bi|0.35 Sb]$_N$/0.3 Bi/2 CoFeB/2 MgO/1 Ta with N = 8 (blue line) and N = 16 (red line). a.u., arbitrary units. (**B**) AFM image of the N = 8 film. A line profile along the blue solid line drawn in the bottom image is shown at the top. (**C**) Cross-sectional HAADF-STEM images of the N = 16 structure. Selected nanobeam diffraction pattern of the Bi|Sb multilayer is shown in the inset.

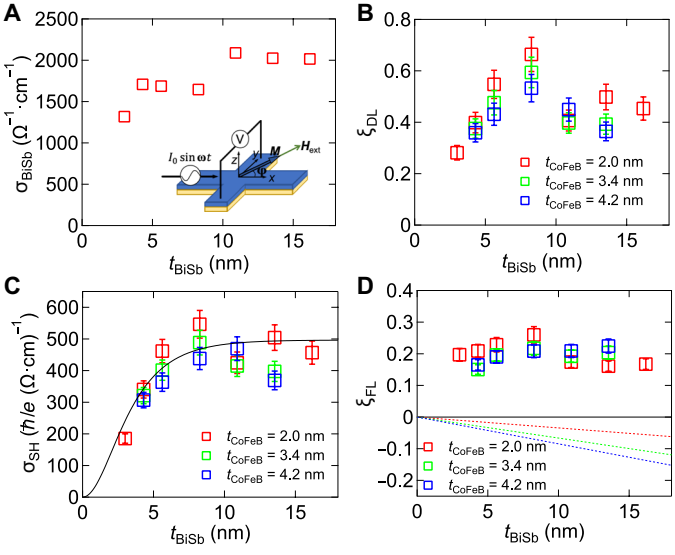

Fig. 2. $Bi_{0.53}Sb_{0.47}$ thickness dependence of SOT and σ_{SH}. (**A**) Conductivity σ_{BiSb} of $Bi_{0.53}Sb_{0.47}$ plotted as a function of its thickness t_{BiSb}. Inset: Schematic illustration of a Hall bar device and the coordinate system. (**B** to **D**) t_{BiSb} dependence of the damping-like spin Hall efficiency ξ_{DL} (B), the SHC σ_{SH} (C), and the field-like spin Hall efficiency ξ_{FL} (D) of t_{BiSb} $Bi_{0.53}Sb_{0.47}/t_{CoFeB}$ CoFeB. Dotted lines represent contributions from the Oersted field. All data were obtained at 300 K.

contributions from each effect (see Materials and Methods for the details). H_{DL} (H_{FL}) is related to the damping-like (field-like) spin Hall efficiency via $\xi_{DL(FL)} = \frac{2e}{\hbar}\frac{H_{DL(FL)} M_s t_{eff}}{j_{BiSb}}$, where j_{BiSb} is the current density in $Bi_{1-x}Sb_x$, and M_s and $t_{eff} \equiv t_{CoFeB} - t_D$ denote the saturation magnetization and the effective thickness of the CoFeB layer, respectively. t_D is the thickness of the magnetic dead layer (see the Supplementary Materials for details of magnetic properties of the films). From here, we discuss the values of ξ_{DL} and ξ_{FL}. To estimate the SHC of $Bi_{1-x}Sb_x$, we use the relation $\sigma_{SH} = \xi_{DL}\sigma_{BiSb}$, where the spin transmission across the $Bi_{1-x}Sb_x$/CoFeB interface is assumed transparent (*19*, *20*, *44*). Taking into account a nontransparent interface will result in larger ξ_{DL} (and likely ξ_{FL}) and therefore results in larger σ_{SH}.

$Bi_{1-x}Sb_x$ thickness dependence of σ_{SH}

We first study the layer thickness dependence of the transport properties of heterostructures with nearly equiatomic $Bi_{0.53}Sb_{0.47}$ ($t_{Bi} \sim t_{Sb} \sim 0.35$ nm). The conductivity of $Bi_{0.53}Sb_{0.47}$ is plotted against t_{BiSb} in Fig. 2A. The slight increase of σ_{BiSb} with t_{BiSb} may be related to the larger grain size of thicker films that reduces the scattering at grain boundaries. Note that σ_{CoFeB} takes an average value of $\sim 5.5 \times 10^3\ \Omega^{-1}\ cm^{-1}$ and shows little dependence on t_{BiSb}. The t_{BiSb} dependence of ξ_{DL} and ξ_{FL} for $Bi_{0.53}Sb_{0.47}$/CoFeB heterostructures measured at 300 K is shown in Fig. 2, B and D, respectively. For a given t_{BiSb}, we studied devices with three different t_{CoFeB} (~2, 3.4, and 4.3 nm). We find that ξ_{DL} of $Bi_{0.53}Sb_{0.47}$ has the same sign with that of Pt (*45*) and is consistent with previous reports on molecular beam epitaxy (MBE)–grown $Bi_{0.9}Sb_{0.1}$ (*31*) and stoichiometric Bi_2Se_3 (*23*, *29*) topological insulators. At $t_{BiSb} \sim 8$ nm, ξ_{DL} reaches a maximum of ~0.65. This value is significantly larger than those found in HMs but lower than some recent reports on Bi-based topological insulators (*23*, *28*, *30*, *31*). ξ_{DL} shows little dependence on t_{CoFeB}, indicating that the CoFeB layer plays little role in setting the SOT of the heterostructures.

To take into account the change of σ_{BiSb} with t_{BiSb}, we plot the SHC $\sigma_{SH} = \xi_{DL}\sigma_{BiSb}$ against t_{BiSb} in Fig. 2C. σ_{SH} increases with increasing t_{BiSb} and tends to saturate beyond t_{BiSb} of ~8 nm. This thickness dependence resembles that expected for the bulk SHE in $Bi_{0.53}Sb_{0.47}$ and is inconsistent with the surface state–dominant scenario (*23*, *46*) or with the quantum confinement picture (*30*). We fit all data using the relation $\sigma_{SH} = \bar{\sigma}_{SH}\left[1 - \mathrm{sech}\left(\frac{t_{BiSb}}{\lambda}\right)\right]$ with the bulk SHC $\bar{\sigma}_{SH}$ and the spin diffusion length λ as the fitting parameters (*47*). We find $\bar{\sigma}_{SH} = 496 \pm 26\,(\hbar/e)\Omega^{-1}\,cm^{-1}$ and $\lambda = 2.3 \pm 0.4$ nm for $Bi_{0.53}Sb_{0.47}$.

Figure 2D illustrates the t_{BiSb} dependence of ξ_{FL} for heterostructures with different CoFeB thicknesses. The contribution from H_{Oe}, which takes the form of $H_{Oe}/j_{BiSb} = 2\pi t_{BiSb}$ [10^{-1} Oe/(A · cm^{-2})] according to Ampère's law, is shown by the dotted lines in Fig. 2D. Note that H_{Oe}, which is negative in our convention, is subtracted from the total field-like SOT to calculate ξ_{FL}. We find that H_{FL} is opposite to the Oersted field and ξ_{FL} takes a constant value of ~0.2 throughout the range of t_{BiSb} studied. The sign of ξ_{FL} for $Bi_{0.53}Sb_{0.47}$/CoFeB agrees with that of metallic Pt/Co/AlO_x (*12*), but is opposite to that found in Bi_2Se_3/NiFe (*23*) and MoS_2/CoFeB (*48*). The nearly constant ξ_{FL} against t_{BiSb} is observed for all structures with different t_{CoFeB}. The distinct t_{BiSb} dependence of ξ_{FL} and ξ_{DL} suggests that the two orthogonal components of SOT originate from phenomena of different characteristic length scales (*11*, *49*).

$Bi_{1-x}Sb_x$ composition and facet dependence of σ_{SH}

The bulk $Bi_{1-x}Sb_x$ alloy is known to be a semiconductor with a small bandgap hosting topological surface states for $0.09 \leq x \leq 0.22$ and is semimetallic for the other compositions (*33*, *34*, *50*, *51*). In an effort to shed light on the origin of the SOT, we investigate the Sb concentration (x) dependence of σ_{SH} and related parameters in 10 $Bi_{1-x}Sb_x$/2 CoFeB heterostructures. To characterize the basic transport properties of the $Bi_{1-x}Sb_x$ alloy, we also deposited and measured stacks without the CoFeB layer (i.e., $t_{CoFeB} = 0$). We have excluded pure Bi ($x = 0$) from this study due to its large sheet resistance (considerably larger than those of the $x \neq 0$ alloys) and island-like morphology, which may result in highly nonuniform current flow within the CoFeB layer. For alloys with $x > 0$, the surface roughness notably improves, as shown in Fig. 1B. Figure 3A shows the x dependence of σ_{BiSb}: σ_{BiSb} increases monotonically with increasing Sb concentration. This is consistent with previous report on the transport properties of the bulk $Bi_{1-x}Sb_x$ alloy (*50*), where it was shown that $Bi_{1-x}Sb_x$ gradually changes from being a semiconductor to a semimetal with increasing Sb concentration. As shown in Fig. 3B, the ordinary Hall coefficient $R_H \equiv R_{xy}t_{BiSb}/H_z$ (H_z is the external field along z) also varies monotonically with increasing x. In our convention, $R_H > 0$ ($R_H < 0$) corresponds to carrier transport being dominated by electrons (holes). We find that the carriers of Bi-rich alloys are electron dominant, whereas the Sb-rich structures are hole dominant, accompanied by a smooth sign change of R_H at $x \sim 0.55$. This reflects the multicarrier nature of the polycrystalline $Bi_{1-x}Sb_x$ films, which have at least one hole and one electron pockets at the Fermi level. We note that this differs from the ternary $(Bi_{1-x}Sb_x)_2Te_3$ topological insulator for which R_H diverges and abruptly changes sign when traversing the Dirac point (*26*).

ξ_{DL}, σ_{SH}, and ξ_{FL} as a function of x for $Bi_{1-x}Sb_x$/2 CoFeB heterostructures are presented in Fig. 3 (C and D). ξ_{DL} and ξ_{FL} increase with increasing Bi concentration, reaching a maximum of $\xi_{DL} \sim 1.2$ and $\xi_{FL} \sim 0.41$ for structures with $x \sim 0.17$, a composition for which

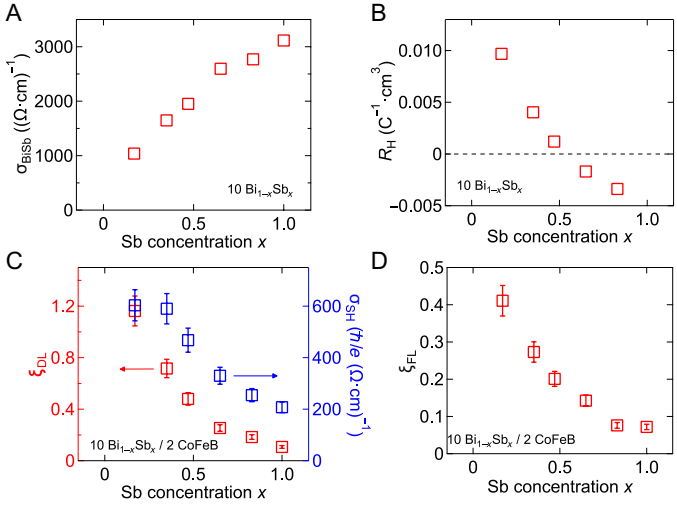

Fig. 3. $Bi_{1-x}Sb_x$ composition dependence of carrier transport and σ_{SH}. (**A** and **B**) Sb concentration *x* dependence of the conductivity σ_{BiSb} (A) and the Hall coefficient R_H (B) of $Bi_{1-x}Sb_x$ with t_{BiSb} = 10 nm. For these studies, heterostructures without the CoFeB layer were used. (**C** and **D**) Sb concentration (*x*) dependence of the damping-like spin Hall efficiency ξ_{DL} (left axis), the SHC σ_{SH} (right axis) (C), and the field-like spin Hall efficiency ξ_{FL} (D) for 10 $Bi_{1-x}Sb_x$/2 CoFeB heterostructures. All data were collected at 300 K.

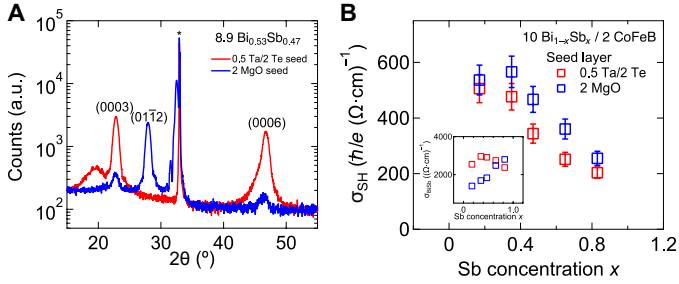

Fig. 4. Facet dependence of σ_{SH}. (**A**) XRD spectra for 8.9 $Bi_{0.53}Sb_{0.47}$ grown on 0.5 Ta/2 Te (red) and 2 MgO (blue) seed layers. Heterostructures without the CoFeB layer were used. (**B**) Sb concentration (*x*) dependence of SHC σ_{SH} for 10 $Bi_{1-x}Sb_x$/2 CoFeB heterostructures with the two seed layers described in (A). The inset shows the *x* dependence of σ_{BiSb}. The measurement temperature is 300 K.

bulk $Bi_{1-x}Sb_x$ is commonly classified as a topological insulator. However, we emphasize that the $Bi_{1-x}Sb_x$ thickness dependence in the previous section and the facet dependence of SHE in the next paragraph both suggest the bulk origin of the SHE. The *x* dependence of σ_{SH} exhibits similar trend with that of ξ_{DL}: We find a plateau of $\sigma_{SH} \sim 600(\hbar/e)\,\Omega^{-1}\,cm^{-1}$ for $x < 0.35$. This *x* dependence of σ_{SH} is in very good agreement with that obtained from tight binding calculations (*38*), suggesting the dominance of the intrinsic contribution over that of the extrinsic skew scattering and side-jump contributions for the observed SHE in $Bi_{1-x}Sb_x$.

We have also varied the seed layer of the $Bi_{1-x}Sb_x$ layer to study the facet-dependent SHE. Figure 4A shows the XRD spectra of 8.9-nm-thick $Bi_{0.53}Sb_{0.47}$ films grown on different seed layers, showing that the orientation of $Bi_{0.53}Sb_{0.47}$ nanocrystallites can be tuned from being practically random ($Bi_{0.53}Sb_{0.47}$ on 0.5 Ta seed; see Fig. 1A) to strongly (0003) oriented (0.5 Ta/2 Te seed) or strongly (01$\bar{1}$2) oriented (2 MgO seed). The Sb concentration (*x*) dependence of the longitudinal conductivity σ_{BiSb} and the SHC of $Bi_{1-x}Sb_x$ are shown in Fig. 4B. As evident from the inset of Fig. 4B, the difference in the texture causes large changes in σ_{BiSb}, particularly at smaller *x*. However, the *x* dependence of SHC hardly changes upon varying the $Bi_{1-x}Sb_x$ texture and σ_{BiSb}. We thus infer that topological surface states, which are intimately related to the $Bi_{1-x}Sb_x$ facets (*34*), are therefore unlikely to be the primary source of the observed SHE. The robustness of SHC against σ_{BiSb} further consolidates our suggestion that the intrinsic mechanism can account for the observed SHE.

Temperature dependence of σ_{SH}

Last, we examine the temperature dependence of the transport properties for $Bi_{1-x}Sb_x$/CoFeB heterostructures with selected *x* ($x \sim 0.17$, 0.47, and 0.65). Here, the seed layer of $Bi_{1-x}Sb_x$ is 0.5 nm Ta. Figure 5A shows σ_{BiSb} as a function of the measurement temperature. We find that $Bi_{1-x}Sb_x$ has weak and positive temperature coefficient of the conductance, which is typical for a semiconductor. To obtain the variation of the carrier concentration and mobility of $Bi_{1-x}Sb_x$, we measured temperature dependence of the longitudinal MR ratio $((R_{xx}(H_z) - R_{xx}(H_z = 0))/R_{xx}(H_z = 0))$ and R_{xy} against H_z. Within the framework of a two-band model (*52*), we define n_h (n_e) as the effective hole (electron) concentration of $Bi_{1-x}Sb_x$, with an effective mobility μ_h (μ_e). Assuming equal population of the two carriers ($n_h = n_e = n$) (*51*), we evaluate these parameters for temperatures ranging from 50 to 300 K, where the MR ratio and R_{xy} are quadratic and linear, respectively, with H_z up to 8 T (see the Supplementary Materials for details of two-band model analysis). The temperature dependence of the carrier concentration and the mobility are summarized in Fig. 5 (B to D). The carrier concentration increases with increasing temperature, which we infer is caused by the thermal broadening of the Fermi-Dirac distribution. In contrast, μ_h and μ_e both decrease with increasing temperature, obeying a power law that scales with $\sim T^{-0.5}$. These results indicate a competition between the impurity-mediated scattering ($\propto T^{1.5}$) and electron-phonon scattering ($\propto T^{-1.5}$), with the latter being more dominant. Compared to the carrier concentration and mobility of the majority carrier for bulk single-crystal Bi ($n \sim 4.6 \times 10^{17}$ cm^{-3}; $\mu_e \sim 6 \times 10^5$ cm^2 V^{-1} s^{-1}) (*53*) and Sb ($n \sim 3.9 \times 10^{19}$ cm^{-3}; $\mu_h \sim 2 \times 10^4$ cm^2 V^{-1} s^{-1}) (*54*) at 77 K, *n* values of the $Bi_{1-x}Sb_x$ films studied here are one to two orders of magnitude higher, while μ values are orders of magnitude lower. These are expected for sputtered polycrystalline thin films that contain significantly higher defect density compared to that of the bulk samples (*36*).

The temperature dependence of ξ_{DL}, σ_{SH}, and ξ_{FL} for 10 $Bi_{1-x}Sb_x$/2 CoFeB heterostructures is plotted in Fig. 5, E to G, respectively. Unexpectedly, all these quantities strongly enhance upon increasing the temperature from 10 K to room temperature (300 K), suggesting that this enhancement is a rather generic feature for the $Bi_{1-x}Sb_x$ alloy. Notably, for $Bi_{0.83}Sb_{0.17}$, up to a threefold (twofold) enhancement is observed for σ_{SH} (ξ_{DL}) over the investigated temperature interval. While similar increase of ξ_{FL} with increasing temperature was previously reported in HM/FM heterostructures (*49*, *55*), this strong enhancement of technologically important ξ_{DL} and σ_{SH} with increasing temperature has not been observed in metallic systems. We have also studied the temperature dependence of σ_{SH} for thinner $Bi_{1-x}Sb_x$ films (5.6 $Bi_{0.53}Sb_{0.47}$/2 CoFeB). We find similar temperature dependence of σ_{SH} compared to that shown in Fig. 5E, which suggests that the temperature dependence of ξ_{DL}, σ_{SH}, and ξ_{FL} is not due to a temperature-dependent spin diffusion length of $Bi_{1-x}Sb_x$. We have also verified that the CoFeB saturation magnetization hardly changes within this temperature range (see the Supplementary

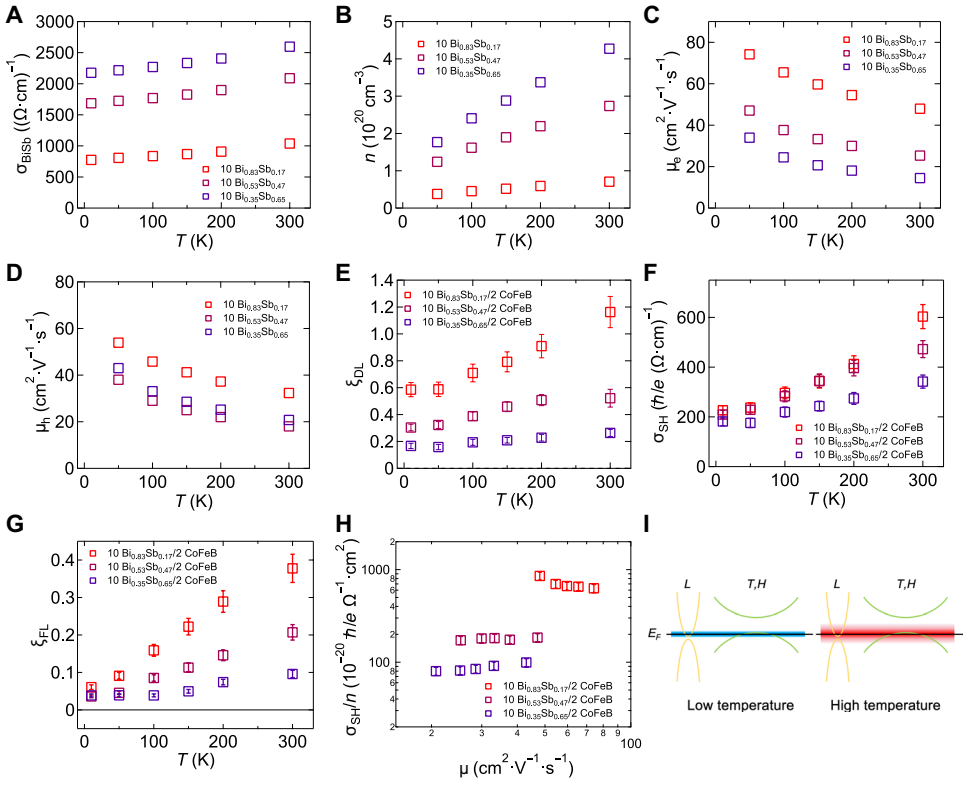

Fig. 5. Temperature dependence of carrier transport and σ_{SH}. (**A** to **D**) Temperature dependence of the conductivity σ_{BiSb} (A), the effective carrier concentration n (B), the electron mobility μ_e (C), and the hole mobility μ_d (D) for 10 $Bi_{1-x}Sb_x$. Heterostructures without the CoFeB layer were used. (**E** to **G**) Temperature dependence of the damping-like spin Hall efficiency ξ_{DL} (E), the SHC σ_{SH} (F), and the field-like spin Hall efficiency ξ_{FL} (G) for 10 $Bi_{1-x}Sb_x$/2 CoFeB heterostructures. (**H**) σ_{SH}/n as a function of the majority carrier mobility (μ_e for $x = 0.17$ and 0.47, and μ_h for $x = 0.65$) for 10 $Bi_{1-x}Sb_x$/2 CoFeB heterostructures. (**I**) Schematic illustration of the band structures of the Bi-rich $Bi_{1-x}Sb_x$ alloy with thermal broadening at low and high temperatures.

Materials), reassuring that the change of ξ_{DL} and ξ_{FL} with temperature is caused by the modulation of the injected spin current.

DISCUSSION

Within the Drude model, the longitudinal conductivity σ_{BiSb} is proportional to the carrier concentration n and the mobility μ. μ is proportional to the relaxation time τ because $\mu = e\tau/m^*$, where m^* is the effective mass. On varying the temperature, contribution from n surpasses that of μ in $Bi_{1-x}Sb_x$, resulting in a positive temperature coefficient of the conductance, as shown in Fig. 5A. For the SHC, by definition, the relaxation time dependence of σ_{SH} provides a measure of the mechanism of the SHE: $\sigma_{SH} \sim \tau^1$ for the extrinsic skew scattering and $\sigma_{SH} \sim \tau^0$ when the intrinsic or side-jump mechanism dominates (*5*). With regard to the relation between σ_{SH} and n, the intrinsic contribution should scale with n if the analogy with the anomalous Hall conductivity applies (*2*). Calculations suggest that similar scaling between σ_{SH} and n holds for the extrinsic mechanisms (*56*). We may thus take the ratio σ_{SH}/n to eliminate the effect of n on the temperature dependence of σ_{SH} . We expect σ_{SH}/n is proportional to μ^1 for the extrinsic skew scattering mechanism and is a constant for the intrinsic/side-jump mechanism. Figure 5H shows σ_{SH}/n as a function of the mobility μ (here, the mobility of the majority carrier is used, i.e., μ_e for $x = 0.17$ and 0.47, and μ_h for $x = 0.65$). We find a relatively weak mobility dependence of σ_{SH}/n for all alloy compositions studied. The slope of σ_{SH}/n versus μ tends to increase as the Sb concentration increases. These results indicate that the extrinsic skew scattering contribution is relatively weak for Bi-rich alloys with large intrinsic SHE, but this contribution becomes nonnegligible (but still smaller than the intrinsic one) with increasing x (and σ_{BiSb}). Although this is reminiscent of the crossover from intrinsic to extrinsic SHE for metallic Pt upon tuning the resistivity of the metal (*57*), we note that σ_{BiSb} at the crossover is one to two orders of magnitude lower than that of Pt. Alternatively, we consider that this crossover is a consequence of the band structure modification induced by Sb doping. As shown in the schematic band structure of Fig. 5I, the transport in the Bi-rich $Bi_{1-x}Sb_x$ alloy is dominated by the Dirac-like electrons at the L point in the momentum space (*33*, *34*, *37*, *50*, *51*). Upon substituting Bi with Sb, holes from the T and H points with quadratic-like dispersion become increasingly important for the conduction, as shown by the x dependence of R_H in Fig. 3B. Our experimental results indicate that Dirac-like L electrons, in contrast to holes in T and H pockets with quadratic dispersion, are key for achieving large intrinsic SHE in $Bi_{1-x}Sb_x$. We thus consider that the large enhancement of SHC with temperature is caused by the increased number of L electrons due to thermal broadening of the Fermi-Dirac distribution.

Referring to the relation between the carrier density, mobility, and conductivity that derives from the Drude model, σ_{SH}/n can be regarded as the equivalent carrier mobility of transverse spin current. To provide reference of the equivalent mobility, we estimate σ_{SH}/n of a typical transition metal, Pt, which has the highest intrinsic

SHC reported thus far [$\sigma_{SH} \approx 2000\ (\hbar/e)\,\Omega^{-1}\,cm^{-1}$ at 0 K (*58*)]. Assuming the carrier density n of Pt is of the order of 10^{22} cm^{-3}, we obtain $\sigma_{SH}/n \sim 20 \times 10^{-20}\ (\hbar/e)\,\Omega^{-1}\,cm^2$. This is more than an order of magnitude smaller than that of $Bi_{0.83}SB_{0.17}$ evaluated at room temperature ($\sigma_{SH}/n \sim 800 \times 10^{-20}\ (\hbar/e)\,\Omega^{-1}\,cm^2$). The difference is also remarkable within the $Bi_{1-x}Sb_x$ alloy. If we compare $Bi_{0.83}Sb_{0.17}$ with $Bi_{0.35}Sb_{0.65}$, although the SHC σ_{SH} differs by a factor of 2, the equivalent mobility σ_{SH}/n is larger for the former by nearly one order of magnitude. These results demonstrate the exceptionally high spin current generation efficiency and mobility of the Dirac-like *L* electrons in Bi-rich $Bi_{1-x}Sb_x$ alloys compared to the majority holes in Sb-rich $Bi_{1-x}Sb_x$ and the predominantly *s*-like conduction electrons in Pt.

In summary, we have studied the SOT in sputter-deposited $Bi_{1-x}Sb_x$/CoFeB heterostructures. The SHC of $Bi_{1-x}Sb_x$ increases with increasing thickness until saturation and is facet independent. These results suggest a dominant contribution from the bulk of the alloy: The effect of the topological surface states, if any, is not evident. The SHC is the largest with Bi-rich composition and decreases with increasing Sb concentration. This trend is in accordance with the intrinsic SHE of $Bi_{1-x}Sb_x$ predicted using tight binding calculations. The SHC and the damping-like spin Hall efficiency increase with increasing temperature. For example, the damping-like spin Hall efficiency of $Bi_{0.83}Sb_{0.17}$ exhibits a twofold enhancement from 5 K to room temperature, reaching $\xi_{DL} \sim 1.2$. We infer that the thermally excited population of the Dirac-like electrons in the *L* valley of the narrow gap $Bi_{1-x}Sb_x$ is responsible for the temperature-dependent SOT. These results show that the Dirac-like electrons in Bi-rich $Bi_{1-x}Sb_x$ alloys are extremely effective in generating spin current, and their equivalent spin current mobility is more than an order of magnitude larger than that of typical transition metals with strong spin-orbit coupling. The very high spin Hall efficiency of Bi-rich $Bi_{1-x}Sb_x$ makes this material an outstanding candidate for applications involving spin current generation and detection at elevated temperatures. In addition, the lower carrier concentration and therefore a smaller electric field screening length in $Bi_{1-x}Sb_x$ compared to the common HMs allow efficient electric field control of SOT, thus paving a route to multifunctional spin-orbitronic devices that are sensitive to external stimuli such as heat and electric field.

MATERIALS AND METHODS

Sample preparation and characterization

All samples were grown at ambient temperature by magnetron sputtering on Si substrates (10×10 mm^2) coated with 100-nm-thick thermally oxidized Si layer. AFM was used to characterize the roughness of the surface. θ – 2θ XRD spectra were obtained using a Cu *Kα* source in parallel beam configuration and with a graphite monochromator on the detector side. The saturation magnetization and the magnetic dead layer thickness of the CoFeB layer in the heterostructures were determined by hysteresis loop measurements using a vibrating sample magnetometer (VSM). AFM, XRD, and VSM studies were performed using unpatterned constant thickness films. HAADF-STEM analysis of cross-sectioned samples was performed using a FEI Titan G2 80-200 TEM with a probe-forming spherical aberration corrector operated at 200 kV. The samples were cross-sectioned from a plain film into thin lamellae by focused ion beam lift-out technique using FEI Helios G4 UX. Hall bars for the transport measurements were pattered from the films using optical lithography and Ar ion etching. The width *w* and the distance between the two longitudinal voltage probes *L* are 10 and 25 μm, respectively. Contact pads to the Hall bars, 10 Ta/100 Au (thickness in nanometers), were formed using a standard lift-off process.

SOT measurements

We treat the CoFeB magnetization as a single domain magnet with a magnetization vector **M** lying in the film plane (*xy* plane) at equilibrium. The external magnetic field H_{ext} is applied along the film plane with an angle φ_H with respect to the *x* axis. We assume that the in-plane magnetic anisotropy of the CoFeB layer is negligible compared to the magnitude of H_{ext}. Thus, the angle φ between **M** and the *x* axis is assumed be equal to φ_H.

When current is passed along *x*, electrons with their spin direction parallel to *y* diffuses into the CoFeB layer via the SHE. The impinging spin current exerts spin-transfer torque (or often referred to as the SOT) on the CoFeB magnetization. The torque can be decomposed into two components, the damping-like and field-like torques: The equivalent effective fields are defined as H_{DL} and H_{FL}, respectively. Together with the Oersted field H_{Oe}, H_{DL} and H_{FL} cause tilting of the CoFeB layer magnetization. When an AC (amplitude I_0, frequency $\omega/2\pi$) is applied to the heterostructure, current-induced oscillation of **M** leads to Hall voltage oscillation via anomalous Hall effect (AHE) and planar Hall effect (PHE). The first harmonic (fundamental) voltage $V_{1\omega}$ represents the magnetization direction at equilibrium, and the out-of-phase second harmonic voltage $V_{2\omega}$ provides information on the current-induced effective fields acting on the magnetization. We define $R_{i\omega} \equiv V_{i\omega}/(I_0/\sqrt{2})$ $(i = 1, 2)$ to represent the harmonic signals.

Contributions to $R_{2\omega}$ include five terms. R_{DL}, R_{FL}, and R_{Oe}, which reflect changes in $R_{2\omega}$ caused by H_{DL}, H_{FL}, and H_{Oe}, respectively, decay with increasing H_{ext}. R_{DL} is proportional to the *x* component of the magnetization (cos φ), whereas $R_{FL} + R_{Oe}$ scales with cos 2 φ cos φ

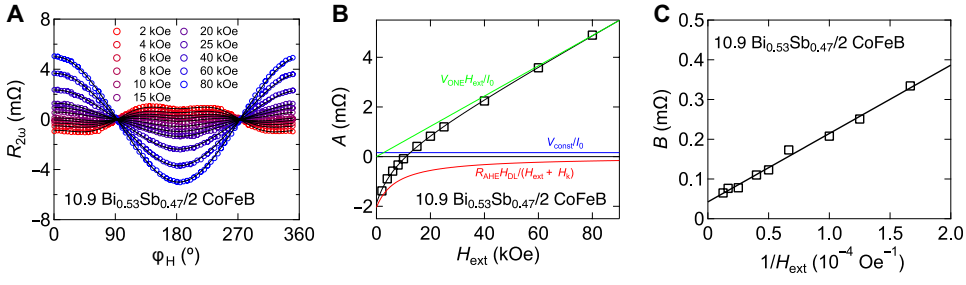

Fig. 6. Representative second harmonic Hall resistances. (**A**) Field angle φ_H dependence of the second harmonic Hall resistance $R_{2\omega}$ for the 10.9 $Bi_{0.53}Sb_{0.47}$/2 CoFeB heterostructure obtained using different H_{ext} measured at 300 K. (**B**) H_{ext} dependence of the fitting parameter *A*. (**C**) $1/H_{ext}$ dependence of the fitting parameter *B*. In (B) and (C), the colored lines show contributions from each component described in Eqs. 2 and 3; the black solid line shows the sum of all contributions.

due to the combined influences of AHE and PHE (*40*, *41*). Current-induced Joule heating and the different thermal conductivity of the substrate and air can lead to an out-of-plane temperature gradient (*41*) across the heterostructure. With the temperature gradient, the ANE of CoFeB and the collective action of the SSE (*59*) in CoFeB followed by the ISHE in $Bi_{1-x}Sb_x$ result in a contribution (R_{const}) that does not depend on the size of H_{ext}. Applying a field orthogonal to the out-of-plane temperature gradient produces the last term, R_{ONE}, due to ONE (*43*). R_{ONE} scales linearly with H_{ext}. ONE of CoFeB is negligible compared to that of $Bi_{1-x}Sb_x$ due to the difference in the carrier density. Both R_{const} and R_{ONE} scale with cos φ.

Putting together these contributions (and assuming $\varphi \sim \varphi_H$), $R_{2\omega}$ reads

$$\begin{aligned} R_{2\omega} &= R_{DL} + R_{ONE} + R_{const} + R_{FL} + R_{Oe} \\ &= \left(R_{AHE}\frac{H_{DL}}{H_{ext}+H_K} + \frac{\mathcal{N}w\Delta T}{I_0}H_{ext} + \frac{\alpha w\Delta T}{I_0}\right)\cos\varphi_H \\ &\quad -2R_{PHE}\frac{H_{FL}+H_{Oe}}{H_{ext}}\cos 2\varphi_H \cos\varphi_H \end{aligned} \quad (1)$$

where R_{AHE} is the anomalous Hall resistance, R_{PHE} is the planar Hall resistance, H_K is the out-of-plane anisotropy field, $\mathcal{N}$ is the ONE coefficient of $Bi_{1-x}Sb_x$, and α is a coefficient that reflects the size of ANE and the combined action of SSE and ISHE. The distinct H_{ext} and φ_H dependence of $R_{2\omega}$ for these contributions allows unambiguous separation of each term from the raw $R_{2\omega}$ signal. We first decompose $R_{2\omega}$ into two contributions of different φ_H dependence, i.e., cos φ_H and cos $2\varphi_H$ cos φ_H, and define the prefactors of these two parts as *A* and *B*, respectively

$$A \equiv R_{AHE}\frac{H_{DL}}{H_{ext}+H_K} + \frac{V_{ONE}}{I_0}H_{ext} + \frac{V_{const}}{I_0} \quad (2)$$

$$B \equiv -2R_{PHE}\frac{H_{FL}+H_{Oe}}{H_{ext}} \quad (3)$$

Two parameters $V_{ONE} \equiv \mathcal{N}w\Delta T$ and $V_{const} \equiv \alpha w\Delta T$ are defined to describe the thermoelectric contributions. The H_{ext} dependence of *A* and *B* is then fitted based on Eqs. 2 and 3, respectively.

Representative $R_{2\omega}$ as a function of φ_H obtained using different H_{ext} for the 10.9 $Bi_{0.53}Sb_{0.47}$/2 CoFeB heterostructure is shown in Fig. 6A. Solid lines in the figure are fits to the data using Eq. 1. See the Supplementary Materials for the φ_H dependence of $R_{1\omega}$. All data shown in this article are collected using $\omega/2\pi = 17.5$ Hz. The current amplitude is typically set to ~1.5 mA_{rms}, which corresponds to a current density in the $Bi_{1-x}Sb_x$ layer of $\sim 1 \times 10^{10}$ A/m^2. We find that $R_{2\omega}$ scales linearly with current. The H_{ext} dependence of one of the fitting parameters *A* is shown in Fig. 6B. The best fit to *A* against H_{ext} is shown by the solid black line. The colored lines represent decomposition of each contribution following Eq. 2 (see the Supplementary Materials for determination of R_{AHE} and H_K). In the small H_{ext} range, R_{DL} term (red line) dominates, whereas at larger field, *A* changes sign and is eventually dominated by R_{ONE} (green line). *B* is plotted against $1/H_{ext}$ in Fig. 6C, with the black solid line showing the best linear fit to the data using Eq. 3. We extract H_{DL}, H_{FL} + H_{Oe}, V_{ONE}, and V_{const} from the two fits. We find V_{const} and V_{ONE} to be proportional to the square of the current flowing within the CoFeB and $Bi_{1-x}Sb_x$ layer, respectively. These results confirm the thermoelectric origin of these contributions and the validity of the interpretation of $R_{2\omega}$.

SUPPLEMENTARY MATERIALS

Supplementary material for this article is available at http://advances.sciencemag.org/cgi/content/full/6/10/eaay2324/DC1

REFERENCES AND NOTES

1. S. Murakami, N. Nagaosa, S.-C. Zhang, Dissipationless quantum spin current at room temperature. *Science* **301**, 1348–1351 (2003).
2. W.-L. Lee, S. Watauchi, V. L. Miller, R. J. Cava, N. P. Ong, Dissipationless anomalous Hall current in the ferromagnetic spinel $CuCr_2Se_{4-x}Br_x$. *Science* **303**, 1647–1649 (2004).
3. M. I. Dyakonov, V. I. Perel, Possibility of orienting electron spins with current. *JETP Lett. USSR* **13**, 467 (1971).
4. J. E. Hirsch, Spin Hall effect. *Phys. Rev. Lett.* **83**, 1834–1837 (1999).
5. J. Sinova, S. O. Valenzuela, J. Wunderlich, C. H. Back, T. Jungwirth, Spin Hall effects. *Rev. Mod. Phys.* **87**, 1213–1260 (2015).
6. Y. A. Bychkov, E. I. Rashba, Properties of a 2d electron-gas with lifted spectral degeneracy. *JETP Lett.* **39**, 78–81 (1984).
7. V. M. Edelstein, Spin polarization of conduction electrons induced by electric current in two-dimensional asymmetric electron systems. *Solid State Commun.* **73**, 233–235 (1990).
8. A. Manchon, H. C. Koo, J. Nitta, S. M. Frolov, R. A. Duine, New perspectives for Rashba spin-orbit coupling. *Nat. Mater.* **14**, 871–882 (2015).
9. L. Liu, C.-F. Pai, Y. Li, H. W. Tseng, D. C. Ralph, R. A. Buhrman, Spin-torque switching with the giant spin Hall effect of tantalum. *Science* **336**, 555–558 (2012a).
10. I. M. Miron, G. Gaudin, S. Auffret, B. Rodmacq, A. Schuhl, S. Pizzini, J. Vogel, P. Gambardella, Current-driven spin torque induced by the Rashba effect in a ferromagnetic metal layer. *Nat. Mater.* **9**, 230–234 (2010).
11. J. Kim, J. Sinha, M. Hayashi, M. Yamanouchi, S. Fukami, T. Suzuki, S. Mitani, H. Ohno, Layer thickness dependence of the current induced effective field vector in Ta | CoFeB | MgO. *Nat. Mater.* **12**, 240–245 (2013).
12. K. Garello, I. M. Miron, C. O. Avci, F. Freimuth, Y. Mokrousov, S. Blugel, S. Auffret, O. Boulle, G. Gaudin, P. Gambardella, Symmetry and magnitude of spin-orbit torques in ferromagnetic heterostructures. *Nat. Nanotechnol.* **8**, 587–593 (2013).
13. I. M. Miron, K. Garello, G. Gaudin, P.-J. Zermatten, M. V. Costache, S. Auffret, S. Bandiera, B. Rodmacq, A. Schuhl, P. Gambardella, Perpendicular switching of a single ferromagnetic layer induced by in-plane current injection. *Nature* **476**, 189–193 (2011).
14. S. Emori, U. Bauer, S.-M. Ahn, E. Martinez, G. S. D. Beach, Current-driven dynamics of chiral ferromagnetic domain walls. *Nat. Mater.* **12**, 611–616 (2013).
15. K.-S. Ryu, L. Thomas, S.-H. Yang, S. Parkin, Chiral spin torque at magnetic domain walls. *Nat. Nanotechnol.* **8**, 527–533 (2013).
16. S. Woo, K. Litzius, B. Kruger, M.-Y. Im, L. Caretta, K. Richter, M. Mann, A. Krone, R. M. Reeve, M. Weigand, P. Agrawal, I. Lemesh, M.-A. Mawass, P. Fischer, M. Kläui, G. S. D. Beach, Observation of room-temperature magnetic skyrmions and their current-driven dynamics in ultrathin metallic ferromagnets. *Nat. Mater.* **15**, 501–506 (2016).
17. H. Nakayama, M. Althammer, Y.-T. Chen, K. Uchida, Y. Kajiwara, D. Kikuchi, T. Ohtani, S. Geprags, M. Opel, S. Takahashi, R. Gross, G. E. W. Bauer, S. T. B. Goennenwein, E. Saitoh, Spin Hall magnetoresistance induced by a nonequilibrium proximity effect. *Phys. Rev. Lett.* **110**, 206601 (2013).
18. Y.-T. Chen, S. Takahashi, H. Nakayama, M. Althammer, S. T. B. Goennenwein, E. Saitoh, G. E. W. Bauer, Theory of spin Hall magnetoresistance. *Phys. Rev. B* **87**, 144411 (2013).
19. J.-C. Rojas-Sanchez, N. Reyren, P. Laczkowski, W. Savero, J. P. Attane, C. Deranlot, M. Jamet, J. M. George, L. Vila, H. Jaffres, Spin pumping and inverse spin Hall effect in platinum: The essential role of spin-memory loss at metallic interfaces. *Phys. Rev. Lett.* **112**, 106602 (2014).
20. W. Zhang, W. Han, X. Jiang, S.-H. Yang, S. S. P. Parkin, Role of transparency of platinum-ferromagnet interfaces in determining the intrinsic magnitude of the spin Hall effect. *Nat. Phys.* **11**, 496–502 (2015).

21. M. Z. Hasan, C. L. Kane, Colloquium: Topological insulators. *Rev. Mod. Phys.* **82**, 3045–3067 (2010).
22. Y. Sun, Y. Zhang, C. Felser, B. Yan, Strong intrinsic spin Hall effect in the TaAs family of Weyl semimetals. *Phys. Rev. Lett.* **117**, 146403 (2016).
23. A. R. Mellnik, J. S. Lee, A. Richardella, J. L. Grab, P. J. Mintun, M. H. Fischer, A. Vaezi, A. Manchon, E. A. Kim, N. Samarth, D. C. Ralph, Spin-transfer torque generated by a topological insulator. *Nature* **511**, 449–451 (2014).
24. Y. B. Fan, P. Upadhyaya, X. F. Kou, M. R. Lang, S. Takei, Z. Wang, J. Tang, L. He, L.-T. Chang, M. Montazeri, G. Q. Yu, W. J. Jiang, T. X. Nie, R. N. Schwartz, Y. Tserkovnyak, K. L. Wang, Magnetization switching through giant spin-orbit torque in a magnetically doped topological insulator heterostructure. *Nat. Mater.* **13**, 699–704 (2014).
25. M. Jamali, J. S. Lee, J. S. Jeong, F. Mahfouzi, Y. Lv, Z. Y. Zhao, B. K. Nikolic, K. A. Mkhoyan, N. Samarth, J.-P. Wang, Giant spin pumping and inverse spin Hall effect in the presence of surface and bulk spin-orbit coupling of topological insulator Bi2se3. *Nano Lett.* **15**, 7126–7132 (2015).
26. K. Kondou, R. Yoshimi, A. Tsukazaki, Y. Fukuma, J. Matsuno, K. S. Takahashi, M. Kawasaki, Y. Tokura, Y. Otani, Fermi-level-dependent charge-to-spin current conversion by Dirac surface states of topological insulators. *Nat. Phys.* **12**, 1027–1031 (2016).
27. K. Yasuda, A. Tsukazaki, R. Yoshimi, K. Kondou, K. S. Takahashi, Y. Otani, M. Kawasaki, Y. Tokura, Current-nonlinear Hall effect and spin-orbit torque magnetization switching in a magnetic topological insulator. *Phys. Rev. Lett.* **119**, 137204 (2017).
28. Y. Wang, D. P. Zhu, Y. Wu, Y. M. Yang, J. W. Yu, R. Ramaswamy, R. Mishra, S. Y. Shi, M. Elyasi, K. L. Teo, Y. H. Wu, H. Yang, Room temperature magnetization switching in topological insulator-ferromagnet heterostructures by spin-orbit torques. *Nat. Commun.* **8**, 1364 (2017).
29. J. H. Han, A. Richardella, S. A. Siddiqui, J. Finley, N. Samarth, L. Q. Liu, Room-temperature spin-orbit torque switching induced by a topological insulator. *Phys. Rev. Lett.* **119**, 077702 (2017).
30. D. C. Mahendra, R. Grassi, J. Y. Chen, M. Jamali, D. R. Hickey, D. L. Zhang, Z. Y. Zhao, H. S. Li, P. Quarterman, Y. Lv, M. Li, A. Manchon, K. A. Mkhoyan, T. Low, J. P. Wang, Room-temperature high spin-orbit torque due to quantum confinement in sputtered $Bi_xSe_{(1-x)}$ films. *Nat. Mater.* **17**, 800–807 (2018).
31. N. H. D. Khang, Y. Ueda, P. N. Hai, A conductive topological insulator with large spin Hall effect for ultralow power spin-orbit torque switching. *Nat. Mater.* **17**, 808–813 (2018).
32. Y. F. Li, Q. L. Ma, S. X. Huang, C. L. Chien, Thin films of topological kondo insulator candidate smb6: Strong spin-orbit torque without exclusive surface conduction. *Sci. Adv.* **4**, eaap8294 (2018).
33. Y. Liu, R. E. Allen, Electronic-structure of the semimetals Bi and Sb. *Phy. Rev. B* **52**, 1566–1577 (1995).
34. J. C. Y. Teo, L. Fu, C. L. Kane, Surface states and topological invariants in three-dimensional topological insulators: Application to $Bi_{1-x}Sb_x$. *Phys. Rev. B* **78**, 045426 (2008a).
35. D. Z. Hou, Z. Qiu, K. Harii, Y. Kajiwara, K. Uchida, Y. Fujikawa, H. Nakayama, T. Yoshino, T. An, K. Ando, X. F. Jin, E. Saitoh, Interface induced inverse spin Hall effect in bismuth/permalloy bilayer. *Appl. Phys. Lett.* **101**, 042403 (2012).
36. H. Emoto, Y. Ando, G. Eguchi, R. Ohshima, E. Shikoh, Y. Fuseya, T. Shinjo, M. Shiraishi, Transport and spin conversion of multicarriers in semimetal bismuth. *Phys. Rev. B* **93**, 174428 (2016).
37. Y. Fuseya, M. Ogata, H. Fukuyama, Spin-Hall effect and diamagnetism of Dirac electrons. *J. Phys. Soc. Jpn.* **81**, 093704 (2012).
38. C. Sahin, M. E. Flatté, Tunable giant spin Hall conductivities in a strong spin-orbit semimetal: Bi(1-x)Sb(x). *Phys. Rev. Lett.* **114**, 107201 (2015).
39. T. Fukazawa, H. Kohno, J. Fujimoto, Intrinsic and extrinsic spin Hall effects of Dirac electrons. *J. Phys. Soc. Jpn.* **86**, 094704 (2017).
40. M. Kawaguchi, K. Shimamura, S. Fukami, F. Matsukura, H. Ohno, T. Moriyama, D. Chiba, T. Ono, Current-induced effective fields detected by magnetotrasport measurements. *Appl. Phys. Express* **6**, 113002 (2013).
41. C. O. Avci, K. Garello, M. Gabureac, A. Ghosh, A. Fuhrer, S. F. Alvarado, P. Gambardella, Interplay of spin-orbit torque and thermoelectric effects in ferromagnet/normal-metal bilayers. *Phys. Rev. B* **90**, 224427 (2014).
42. Y.-C. Lau, M. Hayashi, Spin torque efficiency of Ta, W, and Pt in metallic bilayers evaluated by harmonic Hall and spin Hall magnetoresistance measurements. *Jpn. J. Appl. Phys.* **56**, 0802b5 (2017).
43. N. Roschewsky, E. S. Walker, P. Gowtham, S. Muschinske, F. Hellman, S. R. Bank, S. Salahuddin, Spin-orbit torque and nernst effect in Bi-Sb/Co heterostructures. *Phys. Rev. B* **99**, 195103 (2019).
44. M. Weiler, M. Althammer, M. Schreier, J. Lotze, M. Pernpeintner, S. Meyer, H. Huebl, R. Gross, A. Kamra, J. Xiao, Y.-T. Chen, H. Jiao, G. E. W. Bauer, S. T. B. Goennenwein, Experimental test of the spin mixing interface conductivity concept. *Phys. Rev. Lett.* **111**, 176601 (2013).
45. A. Hoffmann, Spin Hall effects in metals. *IEEE Trans. Magn.* **49**, 5172–5193 (2013).
46. Y. Shiomi, K. Nomura, Y. Kajiwara, K. Eto, M. Novak, K. Segawa, Y. Ando, E. Saitoh, Spin-electricity conversion induced by spin injection into topological insulators. *Phys. Rev. Lett.* **113**, 196601 (2014).
47. L. Q. Liu, C.-F. Pai, D. C. Ralph, R. A. Buhrman, Magnetic oscillations driven by the spin Hall effect in 3-terminal magnetic tunnel junction devices. *Phys. Rev. Lett.* **109**, 186602 (2012).
48. Q. M. Shao, G. Q. Yu, Y.-W. Lan, Y. M. Shi, M. Y. Li, C. Zheng, X. D. Zhu, L. J. Li, P. K. Amiri, K. L. Wang, Strong Rashba-Edelstein effect-induced spin-orbit torques in monolayer transition metal dichalcogenide/ferromagnet bilayers. *Nano Lett.* **16**, 7514–7520 (2016).
49. Y. Ou, C.-F. Pai, S. Shi, D. C. Ralph, R. A. Buhrman, Origin of fieldlike spin-orbit torques in heavy metal/ferromagnet/oxide thin film heterostructures. *Phys. Rev. B* **94**, 140414 (2016).
50. W. M. Yim, A. Amith, Bi-Sb alloys for magneto-thermoelectric and thermomagnetic cooling. *Solid-State Electron.* **15**, 1141–1165 (1972).
51. B. Lenoir, H. Scherrer, T. Caillat, An overview of recent developments for BiSb alloys. *Semiconduc. Semimet.* **69**, 101–137 (2001).
52. Z. W. Zhu, B. Fauque, K. Behnia, Y. Fuseya, Magnetoresistance and valley degree of freedom in bulk bismuth. *J. Phys. Condens. Matter* **30**, 313001 (2018).
53. J.-P. Michenaud, J.-P. Issi, Electron and hole transport in bismuth. *J. Phys. Part C Solid State Phys.* **5**, 3061–3072 (1972).
54. O. Oktu, G. A. Saunders, Galvanomagnetic properties of single-crystal antimony between 77 °K and 273 °K. *Proc. Phys. Soc. London* **91**, 156–168 (1967).
55. J. Kim, J. Sinha, S. Mitani, M. Hayashi, S. Takahashi, S. Maekawa, M. Yamanouchi, H. Ohno, Anomalous temperature dependence of current-induced torques in CoFeB/MgO heterostructures with ta-based underlayers. *Phys. Rev. B* **89**, 174424 (2014).
56. W. K. Tse, S. Das Sarma, Spin Hall effect in doped semiconductor structures. *Phys. Rev. Lett.* **96**, 056601 (2006).
57. E. Sagasta, Y. Omori, M. Isasa, M. Gradhand, L. E. Hueso, Y. Niimi, Y. Otani, F. Casanova, Tuning the spin Hall effect of Pt from the moderately dirty to the superclean regime. *Phys. Rev. B* **94**, 060412 (2016).
58. G. Y. Guo, S. Murakami, T.-W. Chen, N. Nagaosa, Intrinsic spin Hall effect in platinum: First-principles calculations. *Phys. Rev. Lett.* **100**, 096401 (2008).
59. K. Uchida, S. Takahashi, K. Harii, J. Ieda, W. Koshibae, K. Ando, S. Maekawa, E. Saitoh, Observation of the spin seebeck effect. *Nature* **455**, 778–781 (2008).
60. X. D. Xu, K. Mukaiyama, S. Kasai, T. Ohkubo, K. Hono, Impact of boron diffusion at MgO grain boundaries on magneto transport properties of MgO/CoFeB/W magnetic tunnel junctions. *Acta Mater.* **161**, 360–366 (2018).
61. S. Ikeda, K. Miura, H. Yamamoto, K. Mizunuma, H. D. Gan, M. Endo, S. Kanai, J. Hayakawa, F. Matsukura, H. Ohno, A perpendicular-anisotropy cofeb-mgo magnetic tunnel junction. *Nat. Mater.* **9**, 721–724 (2010).
62. J. Sinha, M. Hayashi, A. J. Kellock, S. Fukami, M. Yamanouchi, M. Sato, S. Ikeda, S. Mitani, S. H. Yang, S. S. P. Parkin, H. Ohno, Enhanced interface perpendicular magnetic anisotropy in Ta | CoFeB | MgO using nitrogen doped Ta underlayers. *Appl. Phys. Lett.* **102**, 242405 (2013).
63. J. Kim, P. Sheng, S. Takahashi, S. Mitani, M. Hayashi, Spin Hall magnetoresistance in metallic bilayers. *Phys. Rev. Lett.* **116**, 097201 (2016).
64. S. Cho, S.-H. C. Baek, K. D. Lee, Y. Jo, B. G. Park, Large spin Hall magnetoresistance and its correlation to the spin-orbit torque in W/CoFeB/MgO structures. *Sci. Rep.* **5**, 14668 (2015).
65. M. N. Ali, J. Xiong, S. Flynn, J. Tao, Q. D. Gibson, L. M. Schoop, T. Liang, N. Haldolaarachchige, M. Hirschberger, N. P. Ong, R. J. Cava, Large, non-saturating magnetoresistance in WTe2. *Nature* **514**, 205–208 (2014).
66. Y. Wang, P. Deorani, X. P. Qiu, J. H. Kwon, H. S. Yang, Determination of intrinsic spin Hall angle in pt. *Appl. Phys. Lett.* **105**, 152412 (2014).
67. K.-S. Lee, S.-W. Lee, B.-C. Min, K.-J. Lee, Thermally activated switching of perpendicular magnet by spin-orbit spin torque. *Appl. Phys. Lett.* **104**, 072413 (2014).
68. C.-F. Pai, L. Q. Liu, Y. Li, H. W. Tseng, D. C. Ralph, R. A. Buhrman, Spin transfer torque devices utilizing the giant spin Hall effect of tungsten. *Appl. Phys. Lett.* **101**, 122404 (2012).
69. K. Garello, F. Yasin, S. Couet, L. Souriau, J. Swerts, S. Rao, S. Van Beek, W. Kim, E. Liu, S. Kundu, D. Tsvetanova, K. Croes, N. Jossart, E. Grimaldi, M. Baumgartner, D. Crotti, A. Fumemont, P. Gambardella, G. S. Kar, SOT-MRAM 300mm integration for low power and ultrafast embedded memories, in *2018 IEEE Symposium on VLSI Circuits* (IEEE, 2018), pp. 81–82.

Acknowledgments: We thank Y. Fuseya, H. Kohno, and G. Qu for helpful discussions.
Funding: This work was partly supported by JSPS Grants-in-Aid for Specially Promoted Research (grant no. 15H05702), JST CREST (grant no. JPMJCR19T3), the Casio Science Foundation, and the Center for Spintronics Research Network (CSRN). Z.C. acknowledges financial support from Materials Education program for the future leaders in Research,

Industry, and Technology (MERIT). Y.-C.L. is supported by JSPS International Fellowship for Research in Japan (grant no. JP17F17064). **Author contributions:** Y.-C.L., Z.C., and M.H. planned the study. Z.C. and Y.-C.L. grew the samples, designed the experimental setup, performed electrical measurements, and carried out data analysis. Y.-C.L. performed structural characterization (AFM and XRD), fabricated Hall bar devices, and modeled the system transport properties. X.X., T.O., and K.H. carried out TEM imaging. Z.C. and Y.-C.L. wrote the manuscript with input from M.H. All authors contributed to the discussion of results and commented on the manuscript. **Competing interests:** The authors declare that they have no competing interests. **Data and materials availability:** All data needed to evaluate the conclusions in the paper are present in the paper and/or the Supplementary Materials. Additional data related to this paper may be requested from the authors.

Submitted 31 May 2019
Accepted 27 November 2019
Published 6 March 2020
10.1126/sciadv.aay2324

Citation: Z. Chi, Y.-C. Lau, X. Xu, T. Ohkubo, K. Hono, M. Hayashi, The spin Hall effect of Bi-Sb alloys driven by thermally excited Dirac-like electrons. *Sci. Adv.* **6**, eaay2324 (2020).

The spin Hall effect of Bi-Sb alloys driven by thermally excited Dirac-like electrons

Zhendong Chi, Yong-Chang Lau, Xiandong Xu, Tadakatsu Ohkubo, Kazuhiro Hono and Masamitsu Hayashi

Sci Adv **6** (10), eaay2324.
DOI: 10.1126/sciadv.aay2324